

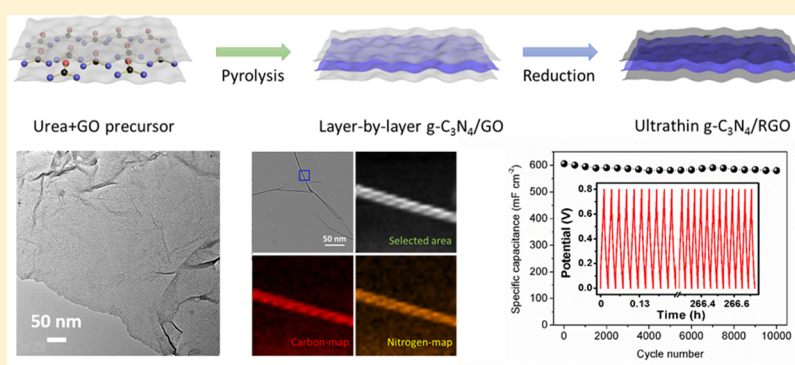
# Ultra-Thin Conductive Graphitic Carbon Nitride Assembly through van der Waals Epitaxy toward High-Energy-Density Flexible Supercapacitors

Chao Lu,<sup>†</sup> Yuan Yang,<sup>‡</sup> and Xi Chen<sup>\*,†</sup>

<sup>†</sup>Department of Earth and Environmental Engineering, Columbia University, New York, New York 10027, United States

<sup>‡</sup>Department of Applied Physics and Applied Mathematics, Columbia University, New York, New York 10025, United States

**S** Supporting Information



**ABSTRACT:** Graphitic carbon nitride is an ordered two-dimensional stability. However, its bulk structure with low electrical conductivity (less than  $1 \text{ S cm}^{-1}$ ) restricts the applications in electrochemical energy storage. This is because conventional synthesis methods lack effective thickness control, and the excessive nitrogen doping ( $\sim 50\%$ ) leads to poor electrical conductivity. Here, we report an ultrathin conductive graphitic carbon nitride assembly (thickness of  $\sim 1.0 \text{ nm}$ ) through graphene-templated van der Waals epitaxial strategy with high electrical conductivity ( $12.2 \text{ S cm}^{-1}$ ), narrow pore-size distribution ( $5.3 \text{ nm}$ ), large surface area ( $724.9 \text{ m}^2 \text{ g}^{-1}$ ), and appropriate nitrogen doping level ( $18.29\%$ ). The ultra-thin structure with nitrogen doping provided numerous channels and active sites for effective ion transportation and storage, while the graphene layers acted as micro current collectors; subsequently, it exhibits high energy storage capability of  $936 \text{ mF cm}^{-2}$  at  $1 \text{ mA cm}^{-2}$  with excellent stability of over 10 000 cycles. Moreover, the all-solid-state supercapacitors showed an ultra-high energy density of  $281.3 \mu\text{Wh cm}^{-2}$  at  $1 \text{ mA cm}^{-2}$  with high rate capability, Coulombic efficiency, and flexibility. This work represents a general framework for the bottom-up synthesis of ultrathin 2D materials, which may promote the application of graphitic carbon nitride in energy storage.

**KEYWORDS:** Graphitic carbon nitride, ultra-thin structure, van der Waals epitaxy, flexible supercapacitors

Graphitic carbon nitride ( $\text{g-C}_3\text{N}_4$ ) is an ordered two-dimensional (2D) semiconducting material with tunable structure, suitable bandgap, high stability, facile synthesis, and low cost.<sup>1–3</sup> Since the first discovery of  $\text{g-C}_3\text{N}_4$  reported by Wang et al. in 2009,<sup>4</sup> tremendous attention has been paid to its applications in photocatalysts, such as water splitting,<sup>5,6</sup> organic pollutant degradation,<sup>7,8</sup> and carbon dioxide reduction.<sup>9</sup> Previous works have demonstrated its potential in solar energy conversion systems; however, its advantages of high nitrogen doping level and 2D layered nanostructures have not yet been fully explored in electrochemical energy storage systems.<sup>1,10</sup> This is mainly because the bulk structural  $\text{g-C}_3\text{N}_4$  materials with low ionic and electrical conductivity is not efficient for ion and electron-transfer kinetics in electrochemical processes.<sup>11,12</sup> Its low conductivity is caused by excessive nitrogen doping level (more than 50%), while the bulk structure always lead to tortuous ion channels with

ineffective ionic migration.<sup>13,14</sup> Thus, the development of high-performance  $\text{g-C}_3\text{N}_4$ -material-based electrodes for electrochemical energy storage is still lacking.

Some attempts have been made to improve electrical conductivity of  $\text{g-C}_3\text{N}_4$  through compositing with conductive materials, such as conductive polymers,<sup>1,15</sup> carbon black,<sup>13,16</sup> CNT,<sup>17</sup> and graphene.<sup>18,19</sup> Although  $\text{g-C}_3\text{N}_4$ -material-based electrodes with improved electric properties could be fabricated, these composite electrodes were still below par for energy storage applications. On the one hand, the weak intermolecular force of the composite often lead to unstable interphase boundaries<sup>20,21</sup> and, thus, fast capacity degradation

**Received:** April 12, 2019

**Revised:** May 14, 2019

**Published:** May 29, 2019

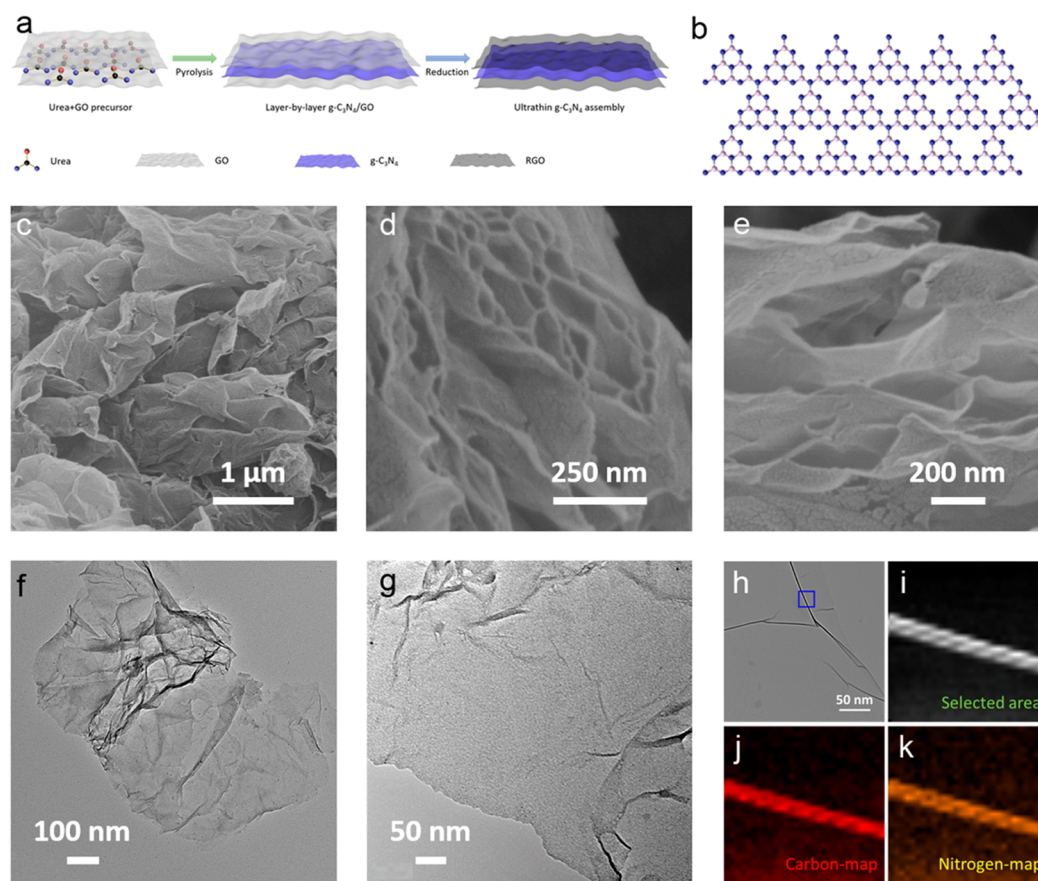


**Figure 1.** Synthesis and morphology characterization of the ultrathin conductive  $g\text{-C}_3\text{N}_4$  assembly. (a) Schematic illustration of the synthesis procedures. (b) Ball-and-stick model of  $g\text{-C}_3\text{N}_4$ . Blue balls represent carbon atoms, while pink balls represent nitrogen atoms. (c–e) SEM images of  $g\text{-C}_3\text{N}_4$  assembly under different magnifications. (f–h) TEM images of  $g\text{-C}_3\text{N}_4$  assembly under different magnifications. (i–k) Scanning TEM image of  $g\text{-C}_3\text{N}_4$  assembly in the selected area of panel h and EDX mappings of carbon and nitrogen element, respectively.

with short lifetime when employed as electrodes for energy storage systems. On the other hand, the bulk structure of  $g\text{-C}_3\text{N}_4$  materials was unfavorable for ion adsorption and conduction because of its low surface area and tortuous ion channels.<sup>3,9</sup> Indeed, the easy formation of bulk structure was mainly resulted from lacking of effective thickness control of conventional synthetic methods, such as hydrothermal and pyrolysis methods,<sup>6,8,10</sup> because the free rotation of single bonds in monomers during reaction tends to form highly cross-linked frameworks rather than the desired 2D planar structure of  $g\text{-C}_3\text{N}_4$ .<sup>7,22,23</sup> Consequently, the synthesis of ultrathin conductive  $g\text{-C}_3\text{N}_4$  assembly with high energy density still remains a challenge.

The epitaxial strategy, a well-known synthetic method for nanomaterials, may be ideal to fill this gap because the interaction between conductive template and monomers largely promotes the in-plane growth of the epilayer rather than out-of-plane cross-linking.<sup>7,24,25</sup> Here, we report the effective synthesis of an ultrathin conductive  $g\text{-C}_3\text{N}_4$  assembly through the graphene templated epitaxial strategy. The atomically flat surface of graphene template favors the in-plane polymerization and achieves layer-by-layer geometry at the molecular level. The self-assembled lamellar structure showed a thickness of about 1.0 nm, average pore size of 5.3 nm, and large surface area of  $724.9 \text{ m}^2 \text{ g}^{-1}$ . The highly conductive graphene component in  $g\text{-C}_3\text{N}_4$  assembly (electrical conductivity of  $12.2 \text{ S cm}^{-1}$ , near 27 times higher than

bulk  $g\text{-C}_3\text{N}_4$ ) could function well as current collector in electrochemical process. The nanoscale dispersion of  $g\text{-C}_3\text{N}_4$  into graphene prevented phase separation during charge–discharge process, making it a robust and long-life electrode material. Additionally, the high level of nitrogen doping (18.29%) provided plenty of chemical anchoring centers by constructing complexing structure with ions for spatial electron transfer in electrochemical process. In a three-electrode system, it exhibited a high energy storage capability of  $936 \text{ mF cm}^{-2}$  at  $1 \text{ mA cm}^{-2}$  with excellent stability over 10 000 cycles thanks to the superior ion and electron transport properties as well as the high nitrogen doping level. The enhanced rate capability and energy storage capacity of  $g\text{-C}_3\text{N}_4$  assembly electrode are mainly deduced from its superior electrical conductivity and high ion-accessible surface area, which were verified by the in situ spectroelectrochemical method. Moreover, all-solid-state supercapacitors based on assembly electrodes exhibited an ultra-high energy density of  $281.3 \mu\text{Wh cm}^{-2}$  at  $1 \text{ mA cm}^{-2}$  with excellent flexibility under bending angles from  $0^\circ$  to  $180^\circ$ . The tunability of the flexible device can be realized through simple cutting method, which may receive potential applications for wearable energy devices. The epitaxial strategy proposed in this work may inspire new design of 2D nanocarbon materials with unique structures and properties for energy storage devices.

Preparation of the ultrathin conductive  $g\text{-C}_3\text{N}_4$  assembly is briefly illustrated in Figure 1a, and the detailed experimental

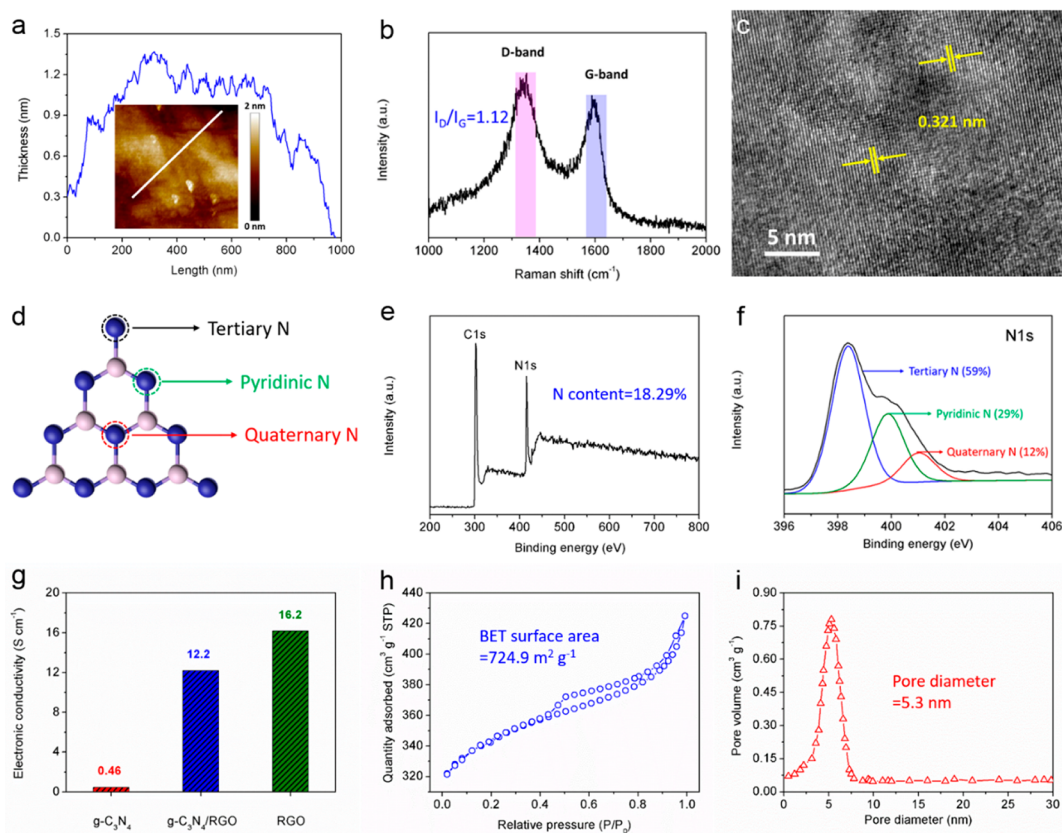


**Figure 2.** Chemical structure analysis of g-C<sub>3</sub>N<sub>4</sub> assembly. (a) Thickness analysis of g-C<sub>3</sub>N<sub>4</sub> assembly. Inset shows the AFM image of material. (b) Raman spectra of g-C<sub>3</sub>N<sub>4</sub> assembly. (c) HRTEM image of g-C<sub>3</sub>N<sub>4</sub> assembly. (d) Schematic for the structure and nitrogen species in g-C<sub>3</sub>N<sub>4</sub>. (e) XPS survey spectra of g-C<sub>3</sub>N<sub>4</sub> assembly. (f) XPS scans for N 1s spectra of g-C<sub>3</sub>N<sub>4</sub> assembly. (g) Comparison of electrical conductivity of g-C<sub>3</sub>N<sub>4</sub>, g-C<sub>3</sub>N<sub>4</sub> assembly and RGO materials. (h) N<sub>2</sub> adsorption/desorption isotherm of g-C<sub>3</sub>N<sub>4</sub> assembly. (i) Pore size distribution of the material.

process is provided in the experimental details. Urea powder was dispersed into graphene oxide through ultrasonic method as a precursor. The strong molecular interactions between urea molecules and surface oxygen-containing groups enabled the uniform dispersion of precursor at the molecular scale, which is beneficial for the following pyrolysis process. As illustrated in Figure S1a, molecular interactions between urea and GO are hydrogen-bond interactions, which is proven by the FTIR spectra in Figure S1b. The peaks of urea spectra at 3100–3600 cm<sup>-1</sup> represented the stretching vibration of hydrogen bonding interactions, whose transmittance intensity enhanced significantly after mixing with graphene oxide to form precursor.<sup>26,27</sup> This strong intermolecular hydrogen-bond interactions weakened out-of-plane bending vibrations of N–H bond at peaks of 650–900 cm<sup>-1</sup>.<sup>28,29</sup> However, the electron inductive effects induced by H-bond enhanced the stretching vibration of the C=O bond (1630–1680 cm<sup>-1</sup>) and the C–N bond (1160 and 1450 cm<sup>-1</sup>) in urea structure.<sup>30,31</sup> Thus, the vibration intensity of chemical bonds reflected by FTIR spectra of contrast samples proved the hydrogen-bond interactions between urea and GO in precursor. Afterward, the precursor was pyrolyzed under argon atmosphere with multi-step temperature programs. Some nitrogen-rich materials have been studied as precursors for synthesis of g-C<sub>3</sub>N<sub>4</sub> under pyrolysis treatment, such as cyanamide, dicyandiamide, melamine, and volatile isocyanic acid.<sup>32–35</sup> However some of these precursors are toxic to humans and the environment, unstable in air, difficult to synthesize on a large scale, and

expensive for mass production. Urea is a cheap and common material in chemical industry and also easy to store because of its chemical stability. It is proven to be an active precursor under thermal treatment for mass production of biuret and melamine, which shows a promising precursor for synthesis of g-C<sub>3</sub>N<sub>4</sub>.<sup>36,37</sup> Based on the advantages of urea comparing with other existing precursors, it was selected as pyrolysis precursor for synthesis of g-C<sub>3</sub>N<sub>4</sub> assembly in this work. Finally, the g-C<sub>3</sub>N<sub>4</sub>/GO intermediate was chemically reduced into g-C<sub>3</sub>N<sub>4</sub> assembly by hydroiodic acid. Chemical structures of g-C<sub>3</sub>N<sub>4</sub> and RGO were shown in Figures 1b and S2. Scanning electron microscopy (SEM) images in Figure 1c–e displayed the layered structure of the g-C<sub>3</sub>N<sub>4</sub> assembly at different magnifications. Transmission electron microscopy (TEM) images in Figure 1f–h clearly showed its ultrathin 2D planar structure. For comparison, the morphology of bulk structural g-C<sub>3</sub>N<sub>4</sub> material was presented in Figure S3. From the energy-dispersive X-ray spectrometry elemental mappings in Figure 1i–k, it can be concluded that the carbon (C) and nitrogen (N) atoms are uniformly distributed in the layer-by-layer structure of the assembly.

To further verify the microstructure of g-C<sub>3</sub>N<sub>4</sub> assembly, structural characterizations using atomic force microscope (AFM), Raman spectra, X-ray diffraction (XRD) pattern, and X-ray photoelectron spectroscopy (XPS) were conducted. According to the AFM result in Figure 2a, the g-C<sub>3</sub>N<sub>4</sub> assembly showed an ultrathin layered structure with average thickness of about 1 nm. The Raman spectra in Figure 2b

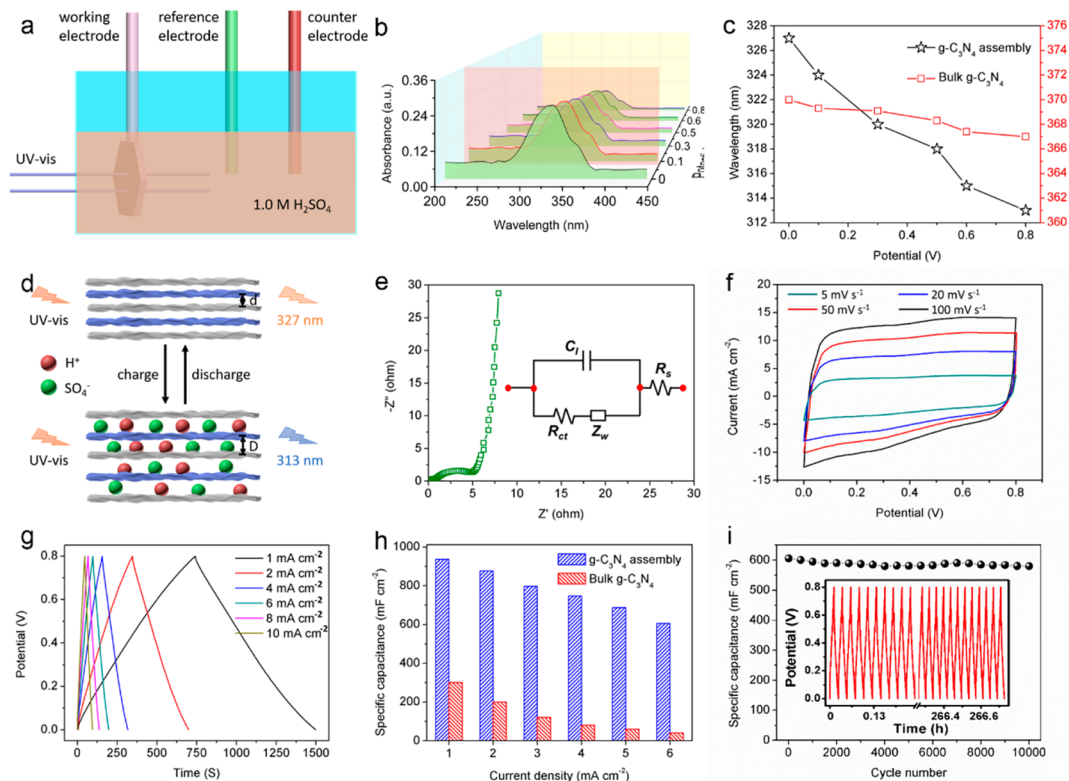


**Figure 3.** Verification of enhanced energy storage mechanism and electrochemical performances of  $g\text{-C}_3\text{N}_4$  assembly by in situ spectroelectrochemical system in  $1.0\text{ M H}_2\text{SO}_4$ . (a) Schematic illustration of the in situ spectroelectrochemical cell. (b) In-situ UV-vis spectra of  $g\text{-C}_3\text{N}_4$  assembly electrode with increasing applied voltages. (c) Potential-dependent absorptivity changes for the peaks of  $g\text{-C}_3\text{N}_4$  assembly and bulk  $g\text{-C}_3\text{N}_4$  electrode, respectively. (d) Schematic for the blue-shift mechanism of the  $g\text{-C}_3\text{N}_4$  assembly electrode. (e) Nyquist plot for  $g\text{-C}_3\text{N}_4$  assembly electrode. Inset shows equivalent circuit. (f) Cyclic voltammograms of  $g\text{-C}_3\text{N}_4$  assembly at various scan rates. (g) Charge-discharge curves of  $g\text{-C}_3\text{N}_4$  assembly at various current densities. (h) Specific capacitances of  $g\text{-C}_3\text{N}_4$  assembly electrodes at different current densities. (i) Cyclic stability of  $g\text{-C}_3\text{N}_4$  assembly at the current density of  $10\text{ mA cm}^{-2}$  for 1000 cycles. Inset shows the charge-discharge cycles.

verified its graphitic structure, whose peaks at  $1349$  and  $1590\text{ cm}^{-1}$  were attributed to the D (disordered and defective structure) and G (graphitic structure) bands.<sup>38,39</sup> The  $I_D$ -to- $I_G$  intensity ratio of  $1.12$  confirmed the high graphitization degree of the assembly. In the XRD pattern of  $g\text{-C}_3\text{N}_4$  assembly in Figure S4, the broad peaks at  $13.1^\circ$  and  $27.5^\circ$  corresponded to the (001) and (002) crystal faces of the assembly, respectively.<sup>40-42</sup> The Fourier transform infrared (FTIR) spectroscopy in Figure S5 displayed the typical molecular structure of  $g\text{-C}_3\text{N}_4$  assembly. The peaks at  $1640.5$ ,  $1569.1$ ,  $1462.1$ , and  $1412.2\text{ cm}^{-1}$  represented typical stretching vibration of heptazine-derived repeating units.<sup>43,44</sup> The peak were assigned to  $812.1\text{ cm}^{-1}$ , the out-of-plane bending vibration characteristic of heptazine rings.<sup>40,45</sup> The peaks at  $1321.8$  and  $1243.3\text{ cm}^{-1}$  corresponded to stretching vibration of connected units of  $\text{C}-\text{N}(-\text{C})-\text{C}$ .<sup>46,47</sup> A broad, weak peak around  $3235.9\text{ cm}^{-1}$  represented the stretching vibration of hydrogen bonding interactions.<sup>22,48</sup> The high-resolution TEM image of the assembly in Figure 2c showed its lamellar structure with adjacent interlayer distances of  $0.321\text{ nm}$ , which was close to the  $d$  spacing of the (002) crystal plane ( $0.324\text{ nm}$ ) in the XRD results.

One structural unit of  $g\text{-C}_3\text{N}_4$  was shown in Figure 2d with three nitrogen (N) species, including pyridinic N, tertiary N, and quaternary N.<sup>49-51</sup> Specifically, the pyridinic N and tertiary N contributed to pseudocapacitive effect in electrochemical system because of the high electron density and electron donating properties.<sup>52,53</sup> The quaternary N may

increase the graphitization degree and electrical conductivity of materials.<sup>54</sup> X-ray photoelectron spectroscopy (XPS) results of  $g\text{-C}_3\text{N}_4$  assembly were presented in Figure 2e,f with a high N doping level achieving  $18.29\%$ . The N 1s signal can be fitted into 3 sub-peaks, including the pyridinic N ( $398.2\text{ eV}$ ), tertiary N ( $399.8\text{ eV}$ ), and quaternary N ( $400.8\text{ eV}$ ).<sup>55,56</sup> The mass percentage of the three N species were  $59\%$ ,  $29\%$ , and  $12\%$ , respectively. It is observed in Figure 2g that electrical conductivity of  $g\text{-C}_3\text{N}_4$  assembly achieved at  $12.2\text{ S cm}^{-1}$ , near 27 times higher than bulk  $g\text{-C}_3\text{N}_4$  ( $0.46\text{ S cm}^{-1}$ ). Characterizations of surface area and porosity of the assembly were illustrated in Figure 2h,i. The specific surface area achieved as high as  $724.9\text{ m}^2\text{ g}^{-1}$ , and the average pore size was  $5.3\text{ nm}$ . In comparison, the surface area of a bulk  $g\text{-C}_3\text{N}_4$  was only  $105.5\text{ m}^2\text{ g}^{-1}$  with a large pore size of  $19.8\text{ nm}$  in Figure S6. The high N doping level, large surface area, and mesopores are expected to improve the ion storage capacity and facilitate the ion- and electron-transport kinetics during electrochemical process.

To classify the role of RGO in conductivity improvement of  $g\text{-C}_3\text{N}_4$  assembly, we prepared contrast sample of RGO/ $g\text{-C}_3\text{N}_4$  physical blend and characterized its microscale morphology and conductivity for comparison. This physical blend gave a much lower conductivity of  $3.4\text{ S cm}^{-1}$  than  $g\text{-C}_3\text{N}_4$  assembly ( $12.2\text{ S cm}^{-1}$ ) but still higher than pure  $g\text{-C}_3\text{N}_4$  materials ( $0.46\text{ S cm}^{-1}$ ). This is because ultra-thin  $g\text{-C}_3\text{N}_4$  assembly synthesized through epitaxy strategy avoided aggregation of  $g\text{-C}_3\text{N}_4$  and form the continuous conductive

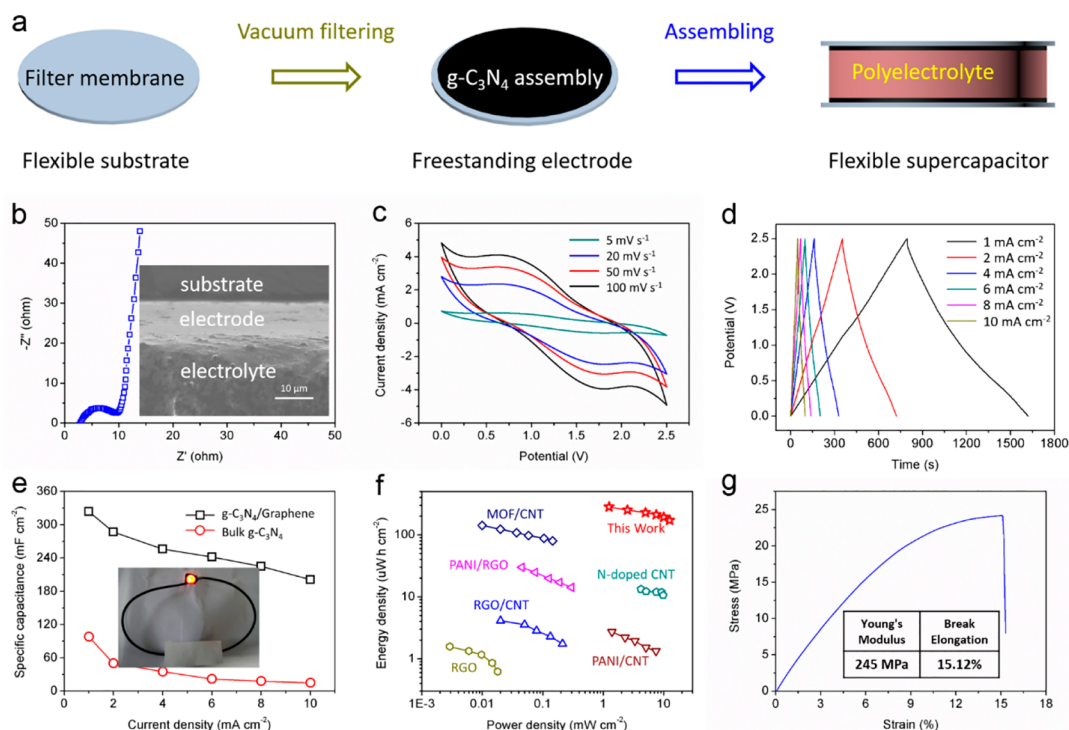


**Figure 4.** Electrochemical properties of a  $g\text{-C}_3\text{N}_4$ -assembly-based supercapacitor. (a) Schematic for the fabrication of supercapacitors. (b) Nyquist plot for the device. The inset is a cross-sectional SEM image of the device. (c) Cyclic voltammograms of device at various scan rates. (d) Charge–discharge curves of device at various current densities. (e) Specific capacitances of the device at different current densities. Inset shows LED light powered by the device. (f) Ragone plot of the  $g\text{-C}_3\text{N}_4$ -assembly-based supercapacitor compared with other devices. (g) Stress–strain curve of the device.

network. However, the RGO/ $g\text{-C}_3\text{N}_4$  physical blend presented serious aggregations and can not form the ultrathin conductive networks, as shown in Figure S7. Thus, the improvement in conductivity of  $g\text{-C}_3\text{N}_4$  assembly is not just due to the existence of RGO but also is mainly attributed to the ultra-thin and continuous conductive network formed through epitaxial strategy.

To verify the enhanced energy storage mechanism of ultrathin  $g\text{-C}_3\text{N}_4$  assembly, in situ spectroelectrochemical method in Figure 3a was used to probe the interfacial interactions between electrodes and ions with increasing voltages. It is well-known that the UV–vis spectra is sensitive to organic conjugate structures, which is suitable for investigating the ionic kinetics of graphitic carbon materials in electrochemical systems.<sup>57–59</sup> The simulated cell was investigated using a standard three-electrode system in 1 M  $\text{H}_2\text{SO}_4$  aqueous solution. Figure 3b showed the spectral changes of the peak centered at 327 nm of  $g\text{-C}_3\text{N}_4$  assembly electrode under various applied voltages. An obvious blue shift of the peak emerged when the applied voltage increased from 0 to 0.8 V, as shown in Figure 3c. This is mainly caused by the immigration of ions into electrode, which weakened the  $\pi\text{-}\pi$  interaction of graphitic layers.<sup>60–62</sup> In contrast, the bulk structural  $g\text{-C}_3\text{N}_4$  electrode tested under the same conditions (Figure S8) had a negligible blue-shift phenomenon of bulk  $g\text{-C}_3\text{N}_4$  electrode, which indicated a much-weaker interaction between ions and bulk  $g\text{-C}_3\text{N}_4$  electrode in an electrochemical system. As shown in Figure 3d, the ultra-thin layered structure ( $\sim 1$  nm) of  $g\text{-C}_3\text{N}_4$  assembly provided numerous channels as ion transport highways, while the graphene components in the assembly functioned as current collectors. The immigrated ions enlarged the interlayer spacing of graphitic layers, which weakened the

$\pi\text{-}\pi$  interactions and thus deduced the blue shift of UV–vis spectra.

The electrochemical energy storage properties of  $g\text{-C}_3\text{N}_4$  assembly electrode was then investigated using three-electrode system in 1 M  $\text{H}_2\text{SO}_4$  electrolyte. Schematic illustration for ionic adsorption state during electrochemical process was displayed in Figure S9a. The graphene layers functioned as conductive pathway for electrons, while the  $g\text{-C}_3\text{N}_4$  layers as adsorption sites for ions. It is noteworthy that the nanoscale dispersion of  $g\text{-C}_3\text{N}_4$  into graphene prevented phase separation during charge–discharge process, making it a robust and long-life electrode material for energy storage. Moreover, the layer-by-layer structures of the assembly provided many more ion channels than the bulk  $g\text{-C}_3\text{N}_4$  (Figure S9b), enabling efficient ion transfer in electrode and promoting the charge–discharge rate during electrochemical process. The numerous vacancies in  $g\text{-C}_3\text{N}_4$  structure, which led to a complexing structure with active ions not only facilitated the spatial electron transfer but also enabled the chemisorption of a large amount of active ions for high capacity (Figure S10). It was also proved by previous works through DFT calculations that  $g\text{-C}_3\text{N}_4$  is an ideal matrix to firmly trap ions due to its high-density N sites and 6-fold cavities.<sup>63,64</sup> The high level of nitrogen doping in the structure acted as chemical anchoring centers, providing strong adsorbability with ions and the pseudocapacitor effect.

From the Nyquist plot of the electrode in Figure 3e, the equivalent series resistance was 4.9 ohms, showing good electrical contact of solid–fluid interface in an aqueous system. In contrast, the bulk  $g\text{-C}_3\text{N}_4$  electrode showed a much higher resistance of 124 ohm due to the absence of intrinsic conductivity in Figure S11. It was observed from the CV curves (Figure 3f) that the regular rectangular shapes with

slight redox peaks demonstrated the capacitive behavior with some Faradaic effects of the assembly.<sup>65,66</sup> The charge–discharge curves in Figure 3g were employed to evaluate the energy storage capacity of g-C<sub>3</sub>N<sub>4</sub> assembly. It exhibited a specific capacitance of 936 mF cm<sup>-2</sup> at the current density of 1 mA cm<sup>-2</sup>, which was much higher than the bulk counterpart in Figure 3h; the CV curves and charge–discharge curves of bulk g-C<sub>3</sub>N<sub>4</sub> electrode were compared in Figure S12. Cycling stability of the electrode was also investigated using charge–discharge test at a current density of 10 mA cm<sup>-2</sup> in Figure 3i. The capacitance value kept retention of above 95% over 10 000 cycles, indicating the excellent cycling stability; however, the bulk structural electrode displayed inferior cycling life showing its unstable structure under electrochemical system (Figure S13). Thus, the present ultra-thin conductive g-C<sub>3</sub>N<sub>4</sub> assembly with excellent energy storage capability may receive promise applications in supercapacitors.

The microscopic flexible 2D layered structure of g-C<sub>3</sub>N<sub>4</sub> assembly made it a promising candidate as electrode material for macroscopic flexible devices. For that matter, a flexible symmetrical supercapacitor was constructed by assembling two electrode layers with one polyelectrolyte layer. The schematic for the assembling process is shown in Figure 4a. The electrode film was fabricated through directly filtering the electrode materials onto the flexible substrate without adding any binder or conductive additive. Optical images of the flexible substrate and electrode were provided in Figure S14. Afterward, the flexible device was assembled by the hot-pressing method. This simple and effective preparation process is also readily scalable. The Nyquist plot of the device is given in Figure 4b. The equivalent series resistance is 9.7 ohm, showing a good interface contact as well as excellent electronic conductivity of electrode. The cross-sectional SEM image in the inset also indicated the fine interface adhesion between electrode and electrolyte layers; in contrast, the bulk g-C<sub>3</sub>N<sub>4</sub> showed a large resistance of 238 ohm due to the intrinsic low electrical conductivity (Figure S15).

Energy storage properties of the device were evaluated by testing the cyclic voltammetry (CV) and charge–discharge curves. The disordered CV curves in Figure 4c verified the typical pseudocapacitive behavior of the g-C<sub>3</sub>N<sub>4</sub> electrode. The charge–discharge curves at various current densities in Figure 4d confirmed the good Coulombic efficiency of device. Although the bulk g-C<sub>3</sub>N<sub>4</sub>-based device also showed the same electrochemical behavior (Figure S16), its energy storage capacity and working stability were greatly inferior. The specific capacitance variation of the two devices in Figure 4e showed that at a current density of 1 mA cm<sup>-2</sup>, the g-C<sub>3</sub>N<sub>4</sub>-assembly-based device exhibited a large specific capacitance of 324 mF cm<sup>-2</sup>, which is 3.3 times larger than that of the bulk g-C<sub>3</sub>N<sub>4</sub>-based one. The former also demonstrated a more stable rate capability, owing to the better ion and electron storage and transport of the ultra-thin conductive g-C<sub>3</sub>N<sub>4</sub> assembly. The RGO components in the g-C<sub>3</sub>N<sub>4</sub> assembly contribute to capacitance with the mechanism of electric double layer capacitance (EDLC). Figure S17a showed the CV curves of RGO-electrode-based supercapacitors at various scan rates and the rectangular shape of these curves verified EDLC energy storage mechanism. The g-C<sub>3</sub>N<sub>4</sub> components contribute with the mechanism of pseudocapacitive capacitance, verified by the redox peaks in CV curves. Charge–discharge curves of the RGO-based device in Figure S17b were used to evaluate the capacitances, as summarized in Figure S17c. At a current

density of 1 mA cm<sup>-2</sup>, the capacitance of the RGO-based device is 143 mF cm<sup>-2</sup>, while that of a g-C<sub>3</sub>N<sub>4</sub>-assembly-based device is 324 mF cm<sup>-2</sup>, which is also higher than the digital sum (241 mF cm<sup>-2</sup>) of RGO- and g-C<sub>3</sub>N<sub>4</sub>-based devices. The additional capacitance was mainly attributed by the ultrathin structure of g-C<sub>3</sub>N<sub>4</sub> assembly with improved surface area for ion storage and conductive network for electron collection and transfer. An LED light powered by our device is presented in the inset. As shown in the Ragone plot in Figure 4f, the energy densities of our device were in the range of 171.9–281.3 μWh cm<sup>-2</sup> at the power densities of 12.5–1.25 mW cm<sup>-2</sup>, which were much higher than previous reported nanocarbon-materials-based devices.<sup>20,67–72</sup>

Stress–strain test was conducted to evaluate the flexibility of the device in Figure 4g, achieving a Young's modulus of 245 MPa and with a break elongation of 15.12%, much higher than previous studies.<sup>73–75</sup> The N-doping level in g-C<sub>3</sub>N<sub>4</sub> assembly have been reduced and controlled through regulating mass ratio of urea to GO precursor in the epitaxial strategy. Urea was used as the nitrogen source, while GO was taken as epitaxial template under pyrolysis treatment. Thus, the N-doping level in g-C<sub>3</sub>N<sub>4</sub> assembly would increase with the increasing mass ratio of urea/GO precursor. Nitrogen active sites in the assembly mainly contribute to pseudocapacitance, while graphene networks provide electron conduction and contribute to electric double layer capacitance. However, to achieve the best energy storage performance for the g-C<sub>3</sub>N<sub>4</sub> assembly electrode, the balance between N doping level and electron conduction of the assembly should be controlled into an optimal value. We have synthesized contrast samples of g-C<sub>3</sub>N<sub>4</sub> assembly with various N doping level through regulating mass ratio of urea/GO precursors before and also measured the corresponding specific capacitances in Figure S18a. Obviously, there is an optimal N doping level for the electrode in the result. When the N doping level was kept at relatively low range, specific capacitance increased with the increasing N doping level because of the increasing pseudocapacitance contributing by N active sites. But excessive N doping level of the assembly would lead to decrease of specific capacitance because the aggregation of g-C<sub>3</sub>N<sub>4</sub> in the assembly blocked the continuous conductive graphene networks, as displayed in the TEM image in Figure S18b.

Previous research reported the thermal oxidation etching method and the liquid-phase exfoliation method for preparing ultra-thin g-C<sub>3</sub>N<sub>4</sub> nanosheets with abundant reactive sites, improved electron transport ability along the in-plane direction, and increased lifetime of photoexcited charge carriers.<sup>76,77</sup> However these pure g-C<sub>3</sub>N<sub>4</sub> nanosheets are still semiconductive materials, which can not be applied as electrode materials because of the poor conductivity, and thus used as photocatalysts. Magnesiothermic denitrating technology was reported for synthesis of low-nitrogen-doping wrinkled graphene nanosheets.<sup>78</sup> However, this technology destroyed intrinsic structure of g-C<sub>3</sub>N<sub>4</sub> and reduced N active sites in-plane direction. This wrinkled graphene showed restacking structures without effective thickness control and led to high equivalent series resistance of 1000 ohm. Epitaxial strategy in our work not only effectively control the thickness of g-C<sub>3</sub>N<sub>4</sub> assembly without destroying its intrinsic structure but also improve the in-plane and out-of-plane directional conductivities. This abundant N active sites accompany with high conductivity made it a promising electrode materials for electrochemical energy storage.

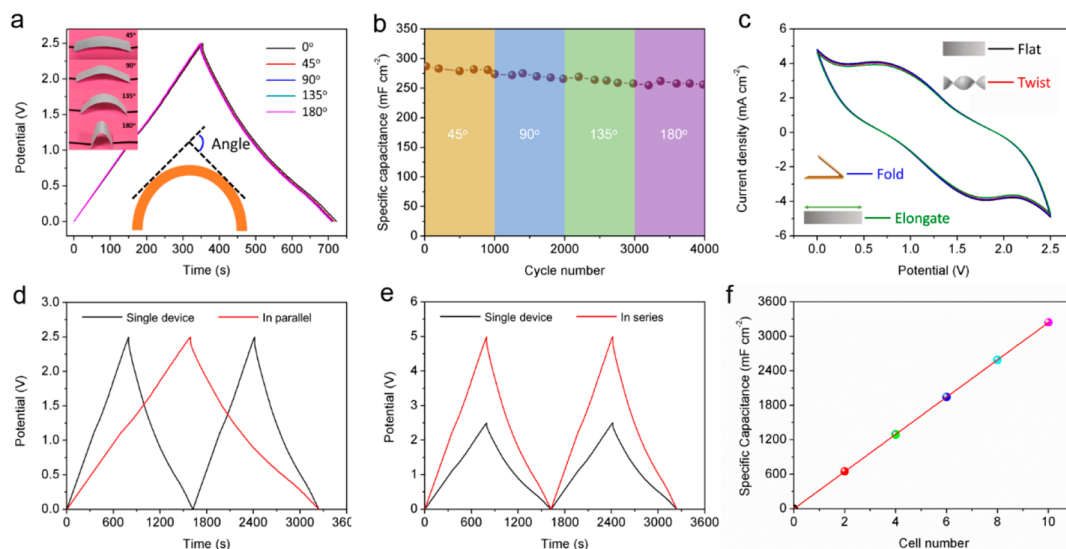


**Figure 5.** Flexibility of  $g\text{-C}_3\text{N}_4$ -assembly-based supercapacitor. (a) Capacitance retention of the device under different bending states ( $0^\circ$ – $180^\circ$ ) at the current density of  $2\text{ mA cm}^{-2}$ . Insets show optical images of the bending devices and angle calculation model. (b) Bending cyclic stability of  $g\text{-C}_3\text{N}_4$ -assembly-based device at a current density of  $2\text{ mA cm}^{-2}$ . (c) CV curves of the device under flattened, twisted, folded, and elongated states at a scan rate of  $5\text{ mV s}^{-1}$ . (d, e) Charge–discharge curves of two devices connected in series and parallel. (f) Relation between total device capacitance and number of devices connected in parallel.

The ability to bear external bending is essential to application of supercapacitor in portable and wearable electronics. To investigate the flexibility of the device, its charge–discharge properties were measured under different bending angles in Figure 5a. The charge–discharge curves showed negligible change under bending angles from  $0^\circ$  to  $180^\circ$  at current density of  $2\text{ mA cm}^{-2}$ , indicating the excellent flexibility of our device. In Figure 5b, the capacitive deterioration were found to be negligible after 1000 repetitive tests under  $45^\circ$ ,  $90^\circ$ ,  $135^\circ$ , and  $180^\circ$ , respectively. Furthermore, the CV curves in Figure 5c under various deformation forms, including twisted, folded, and elongated states, showed negligible change comparing to that of original state, validating its excellent flexibility. To meet the voltage or current needs in practical applications, several devices may need to be integrated in series or parallel, whose equivalent circuit models are shown in Figure S19a,b. When two devices were connected in series (Figure 5d), the output voltage increased from 2.5 to 5.0 V, whereas when they were connected in parallel (Figure 5e), the energy output doubled. The specific capacitance of this integrated system increased linearly with the number of devices in parallel, indicating good scalability (Figure 5f). The editability of flexible electronic devices is crucial to the application in different scenarios, such as attaching, weaving, and other integration forms. Shape design of our supercapacitors were easily realized through a simple cutting method because of its superior robustness and flexibility. As shown in the schematic (Figure S20), our devices could be cut into deferent forms for further integration, including film and fiber states. To verify the potential application of this flexible device, we designed a wearable power supply prototype by integrating three devices into soft fabrics in parallel state, as shown in Figure S21, where the ability of powering a smart watch demonstrated its promise in wearable electronics. We envision that novel devices based on the proposed technique may receive wide application and integration with microelectronic circuits for wearable or implantable micro- and nanoscale devices.

In summary, an ultra-thin conductive graphitic carbon nitride assembly was successfully synthesized through graphene-templated epitaxial strategy. This assembly showed intriguing properties when compared with bulk structural  $g\text{-C}_3\text{N}_4$ , including an ultra-thin 2D structure ( $\sim 1\text{ nm}$ ), high electrical conductivity ( $12.2\text{ S cm}^{-1}$ ), narrow pore-size distribution ( $5.3\text{ nm}$ ), large surface area ( $724.9\text{ m}^2\text{ g}^{-1}$ ), and appropriate nitrogen doping level (18.29%). Based on these merits for effective ion and electron storage and transport dynamics, the  $g\text{-C}_3\text{N}_4$  assembly exhibited high energy storage capability ( $936\text{ mF cm}^{-2}$  at  $1\text{ mA cm}^{-2}$  in a 3-electrode system) with excellent stability over 10 000 cycles. The enhanced energy storage performance of  $g\text{-C}_3\text{N}_4$  assembly electrodes, which resulted from superior electrical conductivity and high ion-accessible surface area, was also verified by the in situ spectroelectrochemical method. Moreover, flexible supercapacitors based on the assembly showed an ultra-high energy density of  $281.3\text{ }\mu\text{Wh cm}^{-2}$  at  $1\text{ mA cm}^{-2}$  with excellent editability for practical wearable applications. This work not only paves the way for the design of competitive electrode materials toward wearable energy applications but also presents a robust and scalable strategy for the bottom-up synthesis of 2D nanocarbon materials with intriguing characteristics for other fields.

## ■ ASSOCIATED CONTENT

### Supporting Information

The Supporting Information is available free of charge on the ACS Publications website at DOI: [10.1021/acs.nanolett.9b01511](https://doi.org/10.1021/acs.nanolett.9b01511).

Additional details on the experimental methods; figures showing intermolecular interactions, FTIR spectra, chemical structures, images of bulk structural  $g\text{-C}_3\text{N}_4$  materials, XRD patterns, nitrogen sorption isotherms, pore size distributions, SEM and TEM images, UV–vis spectral changes, ionic adsorption states, ion channels, experimental compound vacancy, Nyquist plots, cyclic

voltammograms and stability, charge–discharge curves, variations of specific capacitance, equivalent circuit models, supercapacitor schematic integration, and flexible device integration (PDF)

## AUTHOR INFORMATION

### Corresponding Author

\*E-mail: [xichen@columbia.edu](mailto:xichen@columbia.edu).

### ORCID

Yuan Yang: 0000-0003-0264-2640

Xi Chen: 0000-0002-1263-1024

### Notes

The authors declare no competing financial interest.

## ACKNOWLEDGMENTS

This work was supported by the Yonghong Zhang Family Center for Advanced Materials for Energy and Environment and startup funding by Columbia University and AFOSR (grant no. FA9550-18-1-0410).

## REFERENCES

- (1) Tahir, M.; Cao, C.; Mahmood, N.; Butt, F. K.; Mahmood, A.; Idrees, F.; Hussain, S.; Tanveer, M.; Ali, Z.; Aslam, I. *ACS Appl. Mater. Interfaces* **2014**, *6*, 1258–1265.
- (2) Cao, S.; Low, J.; Yu, J.; Jaroniec, M. *Adv. Mater.* **2015**, *27*, 2150–76.
- (3) Song, J.; Yu, Z.; Gordin, M. L.; Wang, D. *Nano Lett.* **2016**, *16*, 864–870.
- (4) Wang, X.; Maeda, K.; Thomas, A.; Takanabe, K.; Xin, G.; Carlsson, J. M.; Domen, K.; Antonietti, M. *Nat. Mater.* **2009**, *8*, 76–80.
- (5) Liu, J. H.; Zhang, Y. W.; Lu, L. H.; Wu, G.; Chen, W. *Chem. Commun.* **2012**, *48*, 8826–8828.
- (6) Yan, S. C.; Li, Z. S.; Zou, Z. G. *Langmuir* **2009**, *25*, 10397–10401.
- (7) Gao, X.; Zhu, Y.; Yi, D.; Zhou, J.; Zhang, S.; Yin, C.; Ding, F.; Zhang, S.; Yi, X.; Wang, J.; Tong, L.; Han, Y.; Liu, Z.; Zhang, J. *Sci. Adv.* **2018**, *4*, eaat6378.
- (8) Chen, X.; Zhang, J.; Fu, X.; Antonietti, M.; Wang, X. *J. Am. Chem. Soc.* **2009**, *131*, 11658–11659.
- (9) Dong, B.; Li, M.; Chen, S.; Ding, D.; Wei, W.; Gao, G.; Ding, S. *ACS Appl. Mater. Interfaces* **2017**, *9*, 17890–17896.
- (10) Dong, G.; Zhang, Y.; Pan, Q.; Qiu, J. *J. Photochem. Photobiol., C* **2014**, *20*, 33–50.
- (11) Xu, Y.; Shi, G.; Duan, X. *Acc. Chem. Res.* **2015**, *48*, 1666–75.
- (12) Tahir, M.; Cao, C.; Butt, F. K.; Idrees, F.; Mahmood, N.; Ali, Z.; Aslam, I.; Tanveer, M.; Rizwan, M.; Mahmood, T. *J. Mater. Chem. A* **2013**, *1*, 13949–13955.
- (13) Fang, Y.; Lv, Y.; Che, R.; Wu, H.; Zhang, X.; Gu, D.; Zheng, G.; Zhao, D. *J. Am. Chem. Soc.* **2013**, *135*, 1524–1530.
- (14) Xiao, M.; Luo, B.; Wang, S.; Wang, L. *J. Energy Chem.* **2018**, *27*, 1111–1123.
- (15) Chen, X.; Zhu, X.; Xiao, Y.; Yang, X. *J. Electroanal. Chem.* **2015**, *743*, 99–104.
- (16) Wang, G.; Zhang, J.; Hou, S. *Mater. Res. Bull.* **2016**, *76*, 454–458.
- (17) Wu, G.; Hu, Y.; Liu, Y.; Zhao, J.; Chen, X.; Whoehling, V.; Plesse, C.; Nguyen, G. T.; Vidal, F.; Chen, W. *Nat. Commun.* **2015**, *6*, 7258–7265.
- (18) Ong, W.-J.; Tan, L.-L.; Chai, S.-P.; Yong, S.-T.; Mohamed, A. R. *Nano Energy* **2015**, *13*, 757–770.
- (19) Chen, Q.; Zhao, Y.; Huang, X.; Chen, N.; Qu, L. *J. Mater. Chem. A* **2015**, *3*, 6761–6766.
- (20) Lu, C.; Wang, D.; Zhao, J.; Han, S.; Chen, W. *Adv. Funct. Mater.* **2017**, *27*, 1606219.
- (21) Liu, J.; Li, W.; Duan, L.; Li, X.; Ji, L.; Geng, Z.; Huang, K.; Lu, L.; Zhou, L.; Liu, Z.; Chen, W.; Liu, L.; Feng, S.; Zhang, Y. *Nano Lett.* **2015**, *15*, 5137–5142.
- (22) Cao, S.; Yu, J. *J. Phys. Chem. Lett.* **2014**, *5*, 2101–2107.
- (23) Li, X.; Cai, W.; An, J.; Kim, S.; Nah, J.; Yang, D.; Piner, R.; Velamakanni, A.; Jung, I.; Tutuc, E.; Banerjee, S. K.; Colombo, L.; Ruoff, R. S. *Science* **2009**, *324*, 1312–1314.
- (24) Ng, H. T.; Li, J.; Smith, M. K.; Nguyen, P.; Cassell, A.; Han, J.; Meyyappan, M. *Science* **2003**, *300*, 1249–1249.
- (25) Peng, X.; Schlamp, M. C.; Kadavanich, A. V.; Alivisatos, A. P. *J. Am. Chem. Soc.* **1997**, *119*, 7019–7029.
- (26) Kundoo, S.; Banerjee, A.; Saha, P.; Chattopadhyay, K. *Mater. Lett.* **2003**, *57*, 2193–2197.
- (27) Ning, L.; De-Ning, W.; Sheng-Kang, Y. *Macromolecules* **1997**, *30*, 4405–4409.
- (28) Jiang, X.; Li, C.; Chi, Y.; Yan, J. *J. Hazard. Mater.* **2010**, *173*, 205–210.
- (29) Madhurambal, G.; Mariappan, M.; Mojumdar, S. *J. Therm. Anal. Calorim.* **2010**, *100*, 763–768.
- (30) Wang, H.-L.; Kao, H.-M.; Digar, M.; Wen, T.-C. *Macromolecules* **2001**, *34*, 529–537.
- (31) Takimiya, K.; Osaka, I.; Nakano, M. *Chem. Mater.* **2014**, *26*, 587–593.
- (32) Groenewolt, M.; Antonietti, M. *Adv. Mater.* **2005**, *17*, 1789–1792.
- (33) Zhang, J.; Chen, X.; Takanabe, K.; Maeda, K.; Domen, K.; Epping, J. D.; Fu, X.; Antonietti, M.; Wang, X. *Angew. Chem., Int. Ed.* **2010**, *49*, 441–444.
- (34) Yan, S.; Li, Z.; Zou, Z. *Langmuir* **2009**, *25*, 10397–10401.
- (35) Lotsch, B. V.; Schnick, W. *Chem. Mater.* **2005**, *17*, 3976–3982.
- (36) Kurzer, F. *Chem. Rev.* **1956**, *56*, 95–197.
- (37) Bann, B.; Miller, S. A. *Chem. Rev.* **1958**, *58*, 131–172.
- (38) Chen, Y.; Fan, Z.; Zhang, Z.; Niu, W.; Li, C.; Yang, N.; Chen, B.; Zhang, H. *Chem. Rev.* **2018**, *118*, 6409–6455.
- (39) Xu, J.; Xu, F.; Qian, M.; Xu, F.; Hong, Z.; Huang, F. *Adv. Mater.* **2017**, *29*, 1701674.
- (40) Liu, J. H.; Zhang, T. K.; Wang, Z. C.; Dawson, G.; Chen, W. *J. Mater. Chem.* **2011**, *21*, 14398–14401.
- (41) Luo, W.; Shen, F.; Bommier, C.; Zhu, H.; Ji, X.; Hu, L. *Acc. Chem. Res.* **2016**, *49*, 231–40.
- (42) Wang, C.; Wang, S.; Chen, G.; Kong, W.; Ping, W.; Dai, J.; Pastel, G.; Xie, H.; He, S.; Das, S.; Hu, L. *Chem. Mater.* **2018**, *30*, 7707–7713.
- (43) Bojdys, M. J.; Müller, J. O.; Antonietti, M.; Thomas, A. *Chem. - Eur. J.* **2008**, *14*, 8177–8182.
- (44) Lotsch, B. V.; Döblinger, M.; Sehnert, J.; Seyfarth, L.; Senker, J.; Oeckler, O.; Schnick, W. *Chem. - Eur. J.* **2007**, *13*, 4969–4980.
- (45) Zheng, Y.; Liu, J.; Liang, J.; Jaroniec, M.; Qiao, S. Z. *Energy Environ. Sci.* **2012**, *5*, 6717–6731.
- (46) Ma, T. Y.; Tang, Y.; Dai, S.; Qiao, S. Z. *Small* **2014**, *10*, 2382–2389.
- (47) Dong, F.; Zhao, Z.; Xiong, T.; Ni, Z.; Zhang, W.; Sun, Y.; Ho, W.-K. *ACS Appl. Mater. Interfaces* **2013**, *5*, 11392–11401.
- (48) Zhang, Y. W.; Liu, J. H.; Wu, G.; Chen, W. *Nanoscale* **2012**, *4*, 5300–5303.
- (49) Sun, Y.; Li, C.; Xu, Y.; Bai, H.; Yao, Z.; Shi, G. *Chem. Commun.* **2010**, *46*, 4740–4742.
- (50) Ge, L.; Han, C. *Appl. Catal., B* **2012**, *117*, 268–274.
- (51) Xiang, Q.; Yu, J.; Jaroniec, M. *J. Phys. Chem. C* **2011**, *115*, 7355–7363.
- (52) Meng, S.; Wu, J.; Zhao, L.; Zheng, H.; Jia, S.; Hu, S.; Meng, W.; Pu, S.; Zhao, D.; Wang, J. *Chem. Mater.* **2018**, *30*, 7306–7312.
- (53) Leube, B. T.; Inglis, K. K.; Carrington, E. J.; Sharp, P. M.; Shin, J. F.; Neale, A. R.; Manning, T. D.; Pitcher, M. J.; Hardwick, L. J.; Dyer, M. S.; Blanc, F.; Claridge, J. B.; Rosseinsky, M. J. *Chem. Mater.* **2018**, *30*, 7183–7200.
- (54) Shao, Y.; El-Kady, M. F.; Sun, J.; Li, Y.; Zhang, Q.; Zhu, M.; Wang, H.; Dunn, B.; Kaner, R. B. *Chem. Rev.* **2018**, *118*, 9233–9280.

- (55) An, S.; Zhang, G.; Wang, T.; Zhang, W.; Li, K.; Song, C.; Miller, J. T.; Miao, S.; Wang, J.; Guo, X. *ACS Nano* **2018**, *12*, 9441–9450.
- (56) Lin, T. Q.; Chen, I. W.; Liu, F. X.; Yang, C. Y.; Bi, H.; Xu, F. F.; Huang, F. Q. *Science* **2015**, *350*, 1508–1514.
- (57) Ryu, W.-H.; Gittleson, F. S.; Thomsen, J. M.; Li, J.; Schwab, M. J.; Brudvig, G. W.; Taylor, A. D. *Nat. Commun.* **2016**, *7*, 12925.
- (58) Li, D.; Müller, M. B.; Gilje, S.; Kaner, R. B.; Wallace, G. G. *Nat. Nanotechnol.* **2008**, *3*, 101.
- (59) Weber, C. M.; Eisele, D. M.; Rabe, J. P.; Liang, Y.; Feng, X.; Zhi, L.; Müllen, K.; Lyon, J. L.; Williams, R.; Bout, D. A. V.; Stevenson, K. J. *Small* **2010**, *6*, 184–189.
- (60) She, X.; Liu, L.; Ji, H.; Mo, Z.; Li, Y.; Huang, L.; Du, D.; Xu, H.; Li, H. *Appl. Catal., B* **2016**, *187*, 144–153.
- (61) Liao, Y.; Zhu, S.; Ma, J.; Sun, Z.; Yin, C.; Zhu, C.; Lou, X.; Zhang, D. *ChemCatChem* **2014**, *6*, 3419–3425.
- (62) Shen, B.; Hong, Z.; Chen, Y.; Lin, B.; Gao, B. *Mater. Lett.* **2014**, *118*, 208–211.
- (63) Yang, W.; Yang, W.; Song, A.; Sun, G.; Shao, G. *Nanoscale* **2018**, *10*, 816–824.
- (64) Zhou, F.; Huang, H.; Xiao, C.; Zheng, S.; Shi, X.; Qin, J.; Fu, Q.; Bao, X.; Feng, X.; Mullen, K.; Wu, Z. S. *J. Am. Chem. Soc.* **2018**, *140*, 8198–8205.
- (65) Lu, C.; Zhao, L.; Hu, Y.; Chen, W. *Chem. Commun.* **2018**, *54*, 8733–8736.
- (66) Stoller, M. D.; Park, S.; Zhu, Y.; An, J.; Ruoff, R. S. *Nano Lett.* **2008**, *8*, 3498–3502.
- (67) Jeong, H. M.; Lee, J. W.; Shin, W. H.; Choi, Y. J.; Shin, H. J.; Kang, J. K.; Choi, J. W. *Nano Lett.* **2011**, *11*, 2472–2477.
- (68) Wu, Y.; Zeng, J.; Si, Y.; Chen, M.; Wu, L. *ACS Nano* **2018**, *12*, 10338–10346.
- (69) Wu, X.; Wu, G.; Tan, P.; Cheng, H.; Hong, R.; Wang, F.; Chen, S. J. *Mater. Chem. A* **2018**, *6*, 8940–8946.
- (70) Beidaghi, M.; Wang, C. *Adv. Funct. Mater.* **2012**, *22*, 4501–4510.
- (71) Dubal, D. P.; Chodankar, N. R.; Caban-Huertas, Z.; Wolfart, F.; Vidotti, M.; Holze, R.; Lokhande, C. D.; Gomez-Romero, P. J. *Power Sources* **2016**, *308*, 158–165.
- (72) Hu, Y.; Cheng, H.; Zhao, F.; Chen, N.; Jiang, L.; Feng, Z.; Qu, L. *Nanoscale* **2014**, *6*, 6448–6451.
- (73) Xu, Z.; Gao, C. *Nat. Commun.* **2011**, *2*, 571.
- (74) Dong, Z.; Jiang, C.; Cheng, H.; Zhao, Y.; Shi, G.; Jiang, L.; Qu, L. *Adv. Mater.* **2012**, *24*, 1856–1861.
- (75) Kou, L.; Huang, T.; Zheng, B.; Han, Y.; Zhao, X.; Gopalsamy, K.; Sun, H.; Gao, C. *Nat. Commun.* **2014**, *5*, 3754.
- (76) Niu, P.; Zhang, L.; Liu, G.; Cheng, H.-M. *Adv. Funct. Mater.* **2012**, *22*, 4763–4770.
- (77) Yang, S.; Gong, Y.; Zhang, J.; Zhan, L.; Ma, L.; Fang, Z.; Vajtai, R.; Wang, X.; Ajayan, P. M. *Adv. Mater.* **2013**, *25*, 2452–6.
- (78) Chen, J.; Mao, Z.; Zhang, L.; Wang, D.; Xu, R.; Bie, L.; Fahlman, B. D. *ACS Nano* **2017**, *11*, 12650–12657.